Geochemistry, Geophysics, Geosystems

RESEARCH ARTICLE
10.1029/2018GC007597

Key Points:
- We studied microseismicity and source mechanisms near the Kishtwar window in the Jammu and Kashmir Himalaya
- Frontal and lateral ramp structures were modeled on the Main Himalayan thrust in this region
- The lateral ramp structure act as heterogeneity controlling the interseismic coupling and give rise to normal faulting

Supporting Information:
- Supporting Information S1
- Table S1
- Table S2

Correspondence to:
H. Paul,
heman2007s@gmail.com

Citation:
Paul, H., Priestley, K. F., Powali, D., Sharma, S., Mitra, S., & Wanchoo, S. K. (2018). Signatures of the existence of frontal and lateral ramp structures near the Kishtwar Window of the Jammu and Kashmir Himalaya: Evidence from microseismicity and source mechanisms. *Geochemistry, Geophysics, Geosystems*, *19*, 3097–3114. https://doi.org/10.1029/2018GC007597

Received 5 APR 2018
Accepted 24 JUL 2018
Accepted article online 14 AUG 2018
Published online 12 SEP 2018

Signatures of the Existence of Frontal and Lateral Ramp Structures Near the Kishtwar Window of the Jammu and Kashmir Himalaya: Evidence From Microseismicity and Source Mechanisms

Himangshu Paul[1,2], Keith Priestley[1], Debarchan Powali[3], Swati Sharma[4], Supriyo Mitra[3], and Sunil Wanchoo[4]

[1]Bullard Laboratories, University of Cambridge, Cambridge, UK, [2]Presently in Institute of Seismological Research, Gandhinagar, India, [3]Department of Earth Science, IISER Kolkata, Mohanpur, India, [4]School of Physics, SMVD University, Katra, India

Abstract We study the Kashmir seismic gap using data from a network of local broadband stations spanning southeastern Kashmir Valley and Jammu. We detected and located several hundred earthquakes using continuous data recorded in our network. The earthquakes (M_L 1.0–5.0) were relocated using probabilistic and relative location methods to obtain a subset of events with depth and spatial uncertainty ≤1.5 km. The earthquakes were found to cluster along two adjacent lines parallel to the strike of the Himalaya but at different depths. The SW cluster was found to be shallower (4–15 km) than the NE cluster (13–18 km). The events in the SW cluster shallowed toward NW from SE. We calculated the source mechanism of larger earthquakes (M_L ≥3.0) using global and local data sets. The source mechanism results show dominant thrust motion of the earthquakes in the NE cluster. Considering nodal planes dipping to the northeast as fault planes, we obtained the model of a steep frontal ramp close to the locked portion of the Main Himalayan Thrust. The model obtained for SW cluster of seismicity showed the presence of a lateral ramp dipping to the SE. Normal faulting was observed in the SW cluster. Our analysis shows two possible causes for the existence of these normal faults—the existing strike-slip motion loading/unloading stresses on the lateral heterogeneities within the decollement or the transfer of potential energy by sediment yield of the river Chenab. The elevated flat situated northwest of the lateral ramp gives rise to very shallow microseismicity (4–7 km).

Plain Language Summary The Indian plate is underthrusting beneath the Eurasian plate. This resulted in the creation of the Himalayas. This underthrusting creates tremendous stress within the contact layer of the two plates known as the decollement. These stresses when released gives rise to megathrust earthquakes. However, there are regions within the Himalaya which have not seen megathrust earthquakes over a period of more than 500 years of recorded history. These regions are called seismic gaps. One such seismic gap lies between the 1905 Kangra earthquake and 2005 Kashmir earthquake regions and is known as the Kashmir seismic gap. We set up a network of seismological stations in the Kashmir seismic gap to understand its nature. We detected several hundred microearthquakes (Magnitude 1.0–5.0) from data recorded in our network. Relocation and focal mechanism study (finding the orientation and slip of the faulting) showed that the earthquakes lie on two specific locations—one shallow (depth 4–15 km) and the other deep (13–18 km) but both lying within the decollement. The foci of the deep earthquakes exhibit a steep frontal ramp in the locked decollement region, whereas shallow earthquakes show a lateral ramp to the southwest. Normal faulting is observed above the lateral ramp structure.

1. Introduction

The convergence of the Indian Plate and the Eurasian Plate takes place along a basal decollement known as the Main Himalayan Thrust (MHT). Approximately, a third of the convergence rate is accomodated within the Himalayan wedge in the form of crustal shortening and moderate seismicity (Bilham et al., 1997). Global Positioning System (GPS) studies have shown that the shallow portion of the MHT is frictionally locked (Bilham et al., 1997; Jouanne et al., 1999; Larson et al., 1999) and accumulates strain during convergence. As the break-

ing stress is exceeded, the Eurasian Plate lurches southward over India resulting in megathrust earthquakes ($M_w \geq 7.5$; Bilham et al., 2001; Molnar, 1987). However, it is not known if every section of the Himalayan arc has produced such megathrust earthquakes. Historical records of major and great earthquakes (Ambraseys & Douglas, 2004; Iyengar et al., 1999) reveal at least two seismic gaps (see inset of Figure 1) where megathrust events have not taken place in the last 500 years (Bilham & Wallace, 2005). These are the eastern Himalayan seismic gap (~250 km along-arc distance between the meizoseismal zones of the 1934 Nepal and 1950 Assam great earthquakes, Ambraseys & Douglas, 2004; Bilham & Wallace, 2005) and the central Himalayan seismic gap (~200-km distance between the 1905 Kangra earthquake rupture area, Wallace et al., 2005, and the overlapped meizoseismal regions of the 1803 Kumaon and 1505 Lo Mustang earthquakes, Ambraseys & Jackson, 2003; Bilham & Wallace, 2005). Similarly, in the western Himalaya, the along-arc region bounded by the rupture zones of 1905 M_W 7.8 Kangra earthquake and the 2005 M_W 7.6 Kashmir earthquake (Kaneda et al., 2008) encompassing the Kashmir Valley, Pir Panjal, and Jammu (Figure 1), is termed as the *Kashmir seismic gap* (Khattri, 1999; Schiffman et al., 2013). The 1905 M_W 7.8 earthquake which ruptured an area of 55×100 km^2 (Figure 1) occurred in the Kangra Valley (Himachal Pradesh) and had a uniform slip of ~4 m (Wallace et al., 2005). The 2005, M_W 7.6 Kashmir earthquake, on the other hand, occurred on the western margin of the Hazara Syntaxis between Bagh and Balakot on multiple faults with its surface rupture (Figure 1) partially following the Main Boundary Thrust (MBT; Avouac et al., 2006; Bendick et al., 2007; Kaneda et al., 2008). It released a ~5.1-m slip on the surface fault and another ~35% of it in the blind wedge thrust beneath the Indus-Kohistan Seismic Zone (IKSZ; Bendick et al., 2007). The Kangra and the Kashmir earthquakes on the southeast and northwest end of the Kashmir seismic gap are the most devastating earthquakes in this region, claiming several tens of thousands lives collectively; however, there has been no evidence of great decollement earthquakes within the gap. The 1555 earthquake, which has a magnitude (M_W) of 7.56 (Ambraseys & Douglas, 2004), may have filled this gap with the SE edge of its rupture area extending up to ~140 km southeast of Srinagar (Ambraseys & Jackson, 2003; Figure 1). However, data from this earthquake are limited to noninstrumental historical records and conclusive inferences about the exact location and rupture area cannot be made. Since then, the Baramulla earthquake of 1885 (M_W 6.3; Ambraseys & Douglas, 2004) is the only strong earthquake to have occurred within this gap.

The Kishtwar Window marks the separation of the Higher Himalayan crystallines from the underlying Lower Himalayan sedimentary/metasedimentary rocks near the Kishtwar region (Singh, 2010; Thakur, 1998). The Kishtwar Window is bounded by the Kishtwar Thrust in the southwest and MCT on the northeast. A plot of seismicity (magnitude ≥ 4.5, depth ≤ 30 km; http://www.isc.ac.uk/iscbulletin/search/catalogue/) in this region (Figure 1) since 1905 reveal that majority of the seismicity is concentrated on the Hazara Syntaxis and the IKSZ. Minor seismicity is observed in the Kashmir seismic gap between the Kishtwar Window and NW edge of the 1905 rupture zone while the rest of the seismic gap seems to be seismically quiet. A few 5+ magnitude earthquakes are observed to have occurred very close to the Kishtwar Window, the latest among them is the 2013 M_W 5.6 earthquake (shown as a blue star in Figure 1). It was a thrust fault occurring at a depth of 16 ± 3 km (Mitra et al., 2014). Interestingly, the past (1980) moderate earthquakes near the Kishtwar Window were also thrusts (shown in pink color in Figure 1, obtained from GCMT catalog). Therefore, it probably is indicative of the activity within the MHT or its splays. This study aims to investigate this particularly active region of the Kashmir seismic gap using data from a focused network of local broadband stations. We detect and locate microearthquakes within a very narrow uncertainty bound to identify active fault planes. It is followed by waveform modeling of larger earthquakes ($M_L \geq 3$) to compute source mechanisms which will help to recognize and understand the nature of deformation going on in this region. Finally, we discuss the local structure, importance of lateral heterogeneities, and possible causes of the seismicity based on our results.

2. Data

To better understand the nature of the Kashmir Seismic gap, a seismological experiment was initiated in this region by the UK-IERI Thematic Partnership between Indian Institute of Science Education and Research Kolkata (IISER-K) and University of Cambridge (CU) in 2011 and later on funded by UGC-UK-IERI and UGC Major Research Project between Shri Mata Vaishno Devi University (SMVDU), IISER-K, and CU. The collaborative details can be found in the Acknowledgments section. The objective of this experiment was to broaden scientific knowledge base and to enable seismic hazard assessment of the region. In the first phase, nine broadband seismological stations were installed spanning Shivalik, Lesser, and Higher Himalaya across Jammu-Kishtwar transect (Figure 1). Stations AKNR, SMVD, NGRT, SUND, and TAPN were installed in the Shivalik Himalaya,

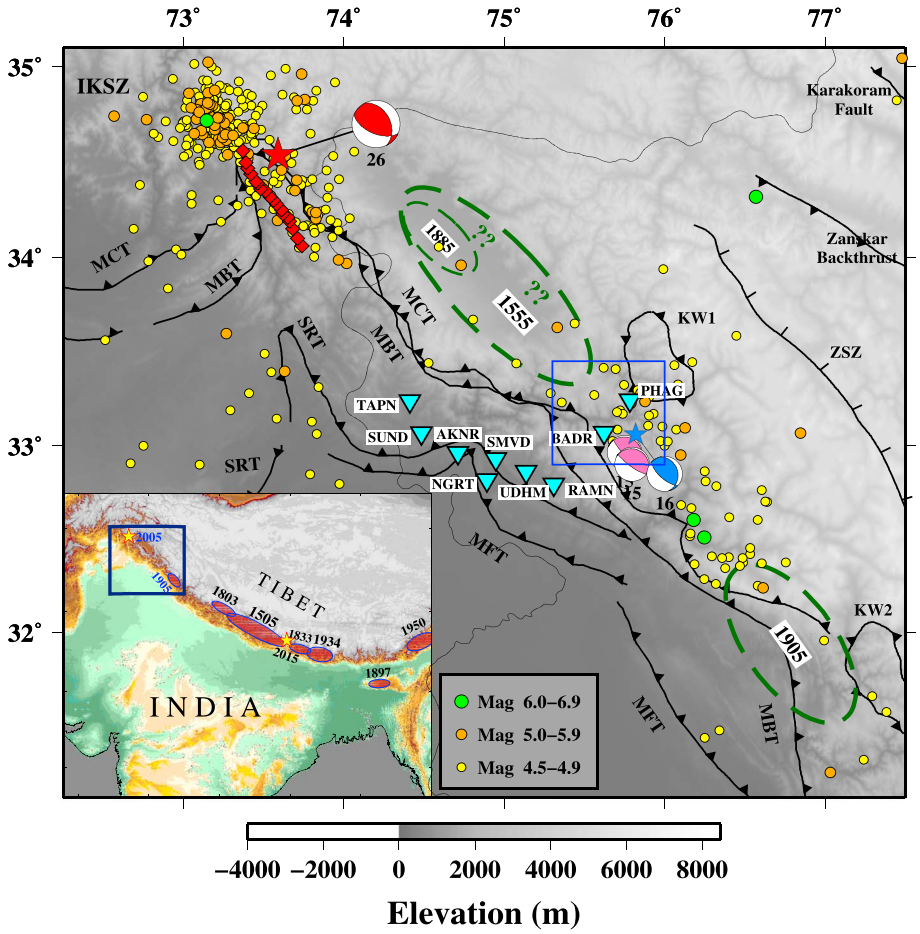

Figure 1. The tectonic map of Jammu and Kashmir Himalaya. The thrust faults and other tectonic features (Avouac et al., 2006; Burg et al., 2005; Searle et al., 1992) are shown as solid black lines. The seismicity in the region since 1905 (ISC reviewed bulletin, magnitude ≥ 4.5, depth ≤ 30 km) is plotted as circles and color coded by magnitude. The shaded green ovals represent approximate rupture area of historical earthquakes—1555, 1885 (Ambraseys & Douglas, 2004; Bilham & Wallace, 2005), 1905 (Szeliga & Bilham, 2017; Wallace et al., 2005). Rupture area of other great earthquakes along the Himalayan arc, viz., 1505, 1833, and 1934 Nepal earthquakes, 1803 Kumaon earthquake, 1897 Shillong, 1950 Assam earthquake (shaded ellipses, approximate area from Bilham & Wallace, 2005), and recent earthquakes like the 2005 Kashmir event and the 2015 Gorkha earthquake (yellow stars) are shown in the inset. The epicenter (NEIC catalog) of 2005 M_W 7.6 Kashmir earthquake is shown as a red star and the surface rupture by aligned red diamonds (Kaneda et al., 2008). The GCMT solution is shown as a beachball (red) representation. The 2013, M_W 5.6 Kishtwar earthquake is shown as a blue star and its source mechanism as a blue beachball (Mitra et al., 2014). Source mechanism (GCMT solution) of two M_W 5.5 earthquakes in 1980 in this region are plotted in pink. The two 6+ magnitude earthquakes (SW of Kishtwar earthquake shown as green circles) occurred in 1914 and 1940, respectively, and therefore their source mechanisms are not available. The blue rectangle denotes the region of observed activity in this study. The inverted triangles (cyan) represent broadband seismological stations whose data have been utilized for this study. MFT = Main Frontal Thrust, MBT = Main Boundary Thrust, MCT = Main Central Thrust, SRT = Salt Range Thrust, KW1 = Kishtwar Window, KW2 = Kulu Window, IKSZ = Indus Kohistan Seismic Zone, ZSZ = Zanskar shear zone.

UDHM and RAMN in the Lesser Himalaya, and BADR and PHAG were situated in the Higher Himalaya. All of these stations were equipped with Güralp CMT-3T/3ESPCD sensors. CMG-3TD seismometers have a flat velocity response between 120 s and 50 Hz whereas CMG-3ESPCD seismometers have flat velocity response between 60 s and 100 Hz. Continuous data were stored in CMG-DCM/EAM data loggers recording at 100 samples per second. The data were time marked by real-time GPS synchronization. These data were used for detecting, locating and waveform modeling of local earthquakes. We also used waveform data from Global Digital Seismic Network (GDSN) stations procured via Incorporated Research Institutions in Seismology (IRIS) Data Management Center (DMC) for computing the source mechanisms of the bigger events ($M_L \geq 4.5$).

3. Earthquake Location

3.1. Automatic Detection and Location

We used continuous data recorded on our local network of stations to detect and locate earthquakes using the Coalescence Microseismic Mapping (CMM) program of Drew et al. (2013). This program consists of two subprograms. The first subprogram is an autopicker, which scans through continuous time series from all stations and triggers for arrival (*P* or *S*) whenever the ratio of short-term average to long-term average (STA/LTA) of the amplitude exceeds a threshold value. The vertical seismogram is band-pass filtered between 2 and 8 Hz while the horizontal seismograms between 1 and 8 Hz to prioritize dominant frequencies of events and attenuate dominant frequencies of noise. Different frequency ranges are chosen such that *P* onsets are dominantly triggered on the vertical component and *S* onsets on the horizontals. The LTA was computed by taking the rms amplitude of a 9-s window preceding the measured data point and the STA as the rms amplitude of a 0.45-s window following the data point. A short STA ensures triggering of short-lasting local earthquakes (Bormann & Wielandt, 2013). We have taken a small value of threshold LTA/STA (2.5) so that we miss very few events. The length of the small and long windows, high- and low-cut filters, and the threshold value were arrived at by trial-and-error tests to detect optimally a high number of events while simultaneously minimizing false triggers (man-made noise, instrumental flickering, etc.) and hence, these values are particularly applicable for our data set and sites.

The second subprogram locates events by coalescing backprojected seismic energy. At first, the study region is divided into a subsurface 3-D grid for a defined velocity model. We selected our study region as a grid of width 400 km in the E-W direction, 300 km in the N-S direction, and a depth of 70 km with 251 gridpoints in each direction. The central grid point of the grid (33.40°N, 75.25°E) was close to the center of our seismological network. Although it is ideal to have the grid region confined to the network of stations only (spanning $\sim 180 \times 50$ km^2, in our case) for better locations, we took a larger grid to test if events from the meizoseismal regions of 2005 Kashmir earthquake and 1905 Kangra earthquake can be detected. The velocity model that we implemented is an average of the velocity structure obtained by joint inversion of receiver function and surface wave dispersion study in this region (Sharma et al., 2018) and is given in Table 1. Once the grid is fixed, a look up table (LUT) is prepared consisting of forward modeled traveltimes (for *P* and *S*) from every station to every grid point. With the help of LUT, the phase onsets from each triggered stations were migrated back to every grid point, for every time step, until they meet at a point which is then considered as the event location. Using this procedure, we detected and located 1,326 earthquakes for a period between July 2013 and June 2014. About 46% of this seismicity was within our network of stations, distributed in the region between Main Frontal Thrust (MFT) and Kishtwar Window. Approximately 39% of the seismicity was found to be in the Hazra Syntaxis and IKSZ, away from our network; we had very little control over the depth uncertainty of these distant events. The rest of the seismicity appeared as several isolated patches in Tibet and Pakistan. We only considered 612 events that occurred within our network for further analysis. A plot of these 612 earthquakes along with their errors in *X*, *Y*, and *Z* directions is shown in Figure S1 in the supporting information.

3.2. Probabilistic Relocation Using Manual Picks

In CMM, the statistical uncertainty in arrival time is measured as a function of the inverse logarithm of the signal-to-noise ratio (SNR; Aki & Richards, 2002) because the probability density function (pdf) represented by the STA/LTA function is proportional to the SNR of the arrivals (Drew et al., 2013). We considered a low-threshold STA/LTA value for maximum detection, but this resulted in a high uncertainty in arrival time and, hence high uncertainty in location of events with low SNR. To constrain the location better and to reduce the overdependence on the SNR, we manually picked *P* and *S* arrivals from each seismogram of the 612 events and entered them into a probabilistic, nonlinear location program called the NonLinLoc (Lomax et al., 2000). Similar to CMM, NonLinLoc also divides the velocity model into a grid and calculates traveltime from each station to all the grid points by a finite difference method (Podvin & Lecomte, 1991). We used a smaller grid of 180 km E-W width, 120 km N-S width, and 40 km depth from the surface with the central grid point at 33.0°N and 75.2°E. The grid cells were also made finer ($0.50 \times 0.50 \times 0.25$ km^3). We used the same velocity model (Sharma et al., 2018) as was used in the first stage of the location procedure. The errors in observed arrival times and the theoretically calculated traveltimes were assumed to be Gaussian in this program, which provided a complete, probabilistic solution for the spatial location in the form of a posterior probability density function (Tarantola & Valette, 1982). The Metropolis-Gibbs algorithm was employed for efficient search of the solution space. Out of the 612 events, 218 events were found to be very well located. They had a maximum uncertainty of ± 1.2 km in longitude, ± 1 km in latitude, and ± 1.5 km in depth. The observed seismicity

Table 1
An Average Velocity Model Obtained From the Joint Inversion of Receiver Function and Surface Wave Dispersion Results of Sharma et al. (2018)

Layer no.	Depth to top of layer (km)	*P* wave velocity (km/s)	*S* wave velocity (km/s)
1.	0.0	4.67	2.56
2.	1.0	4.93	2.68
3.	2.0	5.26	2.86
4.	3.0	5.38	2.92
5.	4.0	5.98	3.25
6.	5.0	6.13	3.34
7.	6.0	5.87	3.19
8.	8.0	5.42	2.95
9.	10.0	5.51	3.00
10.	12.0	5.65	3.07
11.	14.0	5.81	3.16
12.	16.0	6.06	3.29
13.	18.0	5.98	3.25
14.	20.0	6.29	3.42
15.	22.0	6.01	3.27
16.	24.0	6.07	3.30
17.	26.0	6.34	3.45
18.	28.0	6.66	3.62
19.	30.0	6.44	3.50
20.	32.0	6.71	3.65
21.	34.0	6.53	3.55
22.	36.0	6.89	3.74
23.	38.0	7.14	3.88
24.	40.0	7.23	3.93
25.	42.0	7.17	3.90
26.	44.0	6.91	3.76
27.	46.0	6.77	3.68
28.	48.0	6.81	3.70
29.	50.0	7.20	3.92
30.	52.0	7.68	4.18
31.	54.0	7.97	4.33

Note. This velocity model is formed by combining the velocity models from stations SMVD, PHAG, BADR, TAPN, UDHM, and AKNR.

was found to be grouped into two adjacent clusters aligned along axes parallel to the deformation front and located between the Main Central Thrust (MCT) and Kishtwar Window (Figure 2). The cluster to the NE had a depth distribution of ~4–18 km, while the cluster to the SW was comparatively shallow (4–15 km). A few stray events were also observed farther southwest.

To calculate the local magnitude (M_L) of events, we used the relation of Hutton and Boore (1987) given by

$$M_L = \log(A) + 1.110\log(r/100) + 0.00189(r - 100) + 3.0 \quad (1)$$

where A is the maximum amplitude of the Wood-Anderson's seismometer and r is the hypocentral distance. We first deconvolved the instrument response from our seismograms, reconvolved them with the Wood-Anderson response and then measured the half height of the maximum peak-to-peak amplitude on the horizontal components. However, this magnitude (equation (1)) is accurate only for regions which have

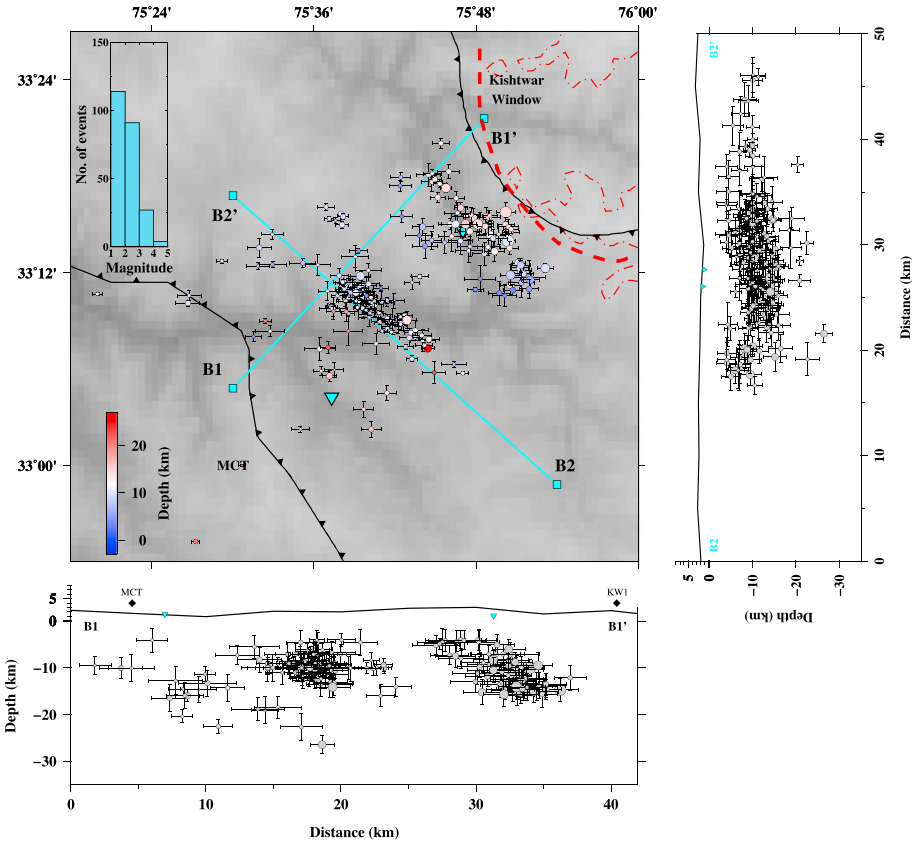

Figure 2. The events relocated by NonLinloc (Lomax et al., 2000) are shown on map and cross section along profiles perpendicular (B1–B1′) and parallel (B2–B2′) to the deformation front, respectively. The cyan triangles represent stations. The error bars show uncertainty of location in *X* (longitude), *Y* (latitude), and *Z* (depth) direction. Only those events were included whose uncertainty in each of *X*, *Y*, and *Z* directions were ≤1.2 km, 1 km, and 1.5 km, respectively. The events are color coded by depth in map view. The actual 3.5-km elevation contours are shown by thin dash-dotted lines (red). The representative 3.5 elevation contour is approximated from the actual contours and is represented by thick red dashed line. The geological features—Main Central Thrust and Kishtwar Window (KW1)—are marked in the cross section by diamonds (blue). The magnitude histogram is shown in the inset.

similar attenuation characteristics as southern California. To account for this, we modify the amplitude measurements by multiplying them with a scalar based on the attenuation relation obtained for the Himalaya (Szeliga et al., 2010). The best located events were between M_L 1.0 and M_L 5.0 with the median M_L equal to 2.3. The magnitude histogram is shown in Figure 2 as an inset.

3.3. Relative Locations

Relative locations further refine the resolution of the hypocenters and can align the diffused seismicity along active fault lineations or narrow planar brittle zones. We use the double-difference algorithm of Waldhauser and Ellsworth (2000) (HypoDD) to improve the location precision. This method is based on the principle that the difference in traveltimes of two nearby events can be attributed to their spatial offset if their separation is small compared to the station-event distance and length of velocity heterogeneity. At first, a network of pairwise connected events is created with a finite number of neighbors to each event within a given search radius. Outlier events, whose delay times exceed maximum expected delay are eliminated. Then the differential predicted and observed traveltimes of all pairs of earthquakes are minimized by adjusting their hypocenters vectorially using the single value decomposition (SVD) method. This is done iteratively with maximum hypocentral separation between pairs, threshold residual time, and distance weighting, decreasing gradually in each iteration. This results in a decreasing number of events but high precision of the remaining events in the clusters.

In addition to arrival times from catalogs, accurate relative arrival timings obtained by cross-correlating waveforms were also provided to increase location precision. Accurate relative timings were obtained by applying

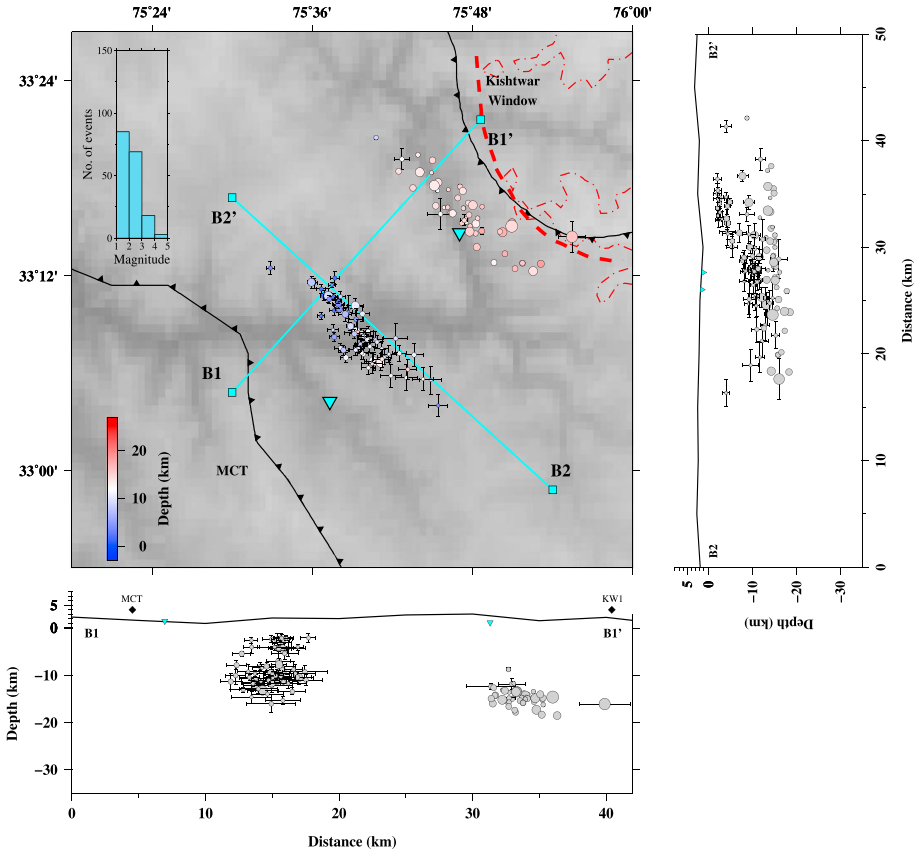

Figure 3. The events relocated by HypoDD (Waldhauser & Ellsworth, 2000) are shown on the map and cross section along profiles perpendicular (B1 – B1′) and parallel (B2 – B2′) to the deformation front, respectively. The cyan triangles represent stations. The error bars represent the uncertainty in location with respect to the cluster center. The events are color coded by depth in map view. The actual 3.5-km elevation contours are shown by thin dash-dotted lines (red). The representative 3.5-km elevation contour is approximated from the actual contours and is represented by thick red dashed line. The known geological features — Main Central Thrust and Kishtwar Window (KW1) are marked in the cross section by diamonds (blue). The magnitude histogram is shown in the inset.

a band-pass filter of corners 0.5 and 8 Hz on the waveforms and cross correlating with one another over a window of 0.5 s preceding the marked arrival time and 5 s following it. We start the relative locations with 218 events obtained from NonLinLoc. At each iteration, the maximum separation between the linked pairs and the threshold residual time were reduced gradually from 5 to 1 km and 0.5 to 0.01 s, respectively. Most of the shallow earthquakes in the NE cluster manifested as airquakes. In total, 62 airquakes were produced during the iterations. This is supported by the fact that we had the largest uncertainty in the *Z* direction. The isolated events and other events from the two clusters were deleted due to the iterative reweighing, change in distance separation, and residual time. The large number of event deletion could be due to the large separation between the two clusters of seismicity which reduces the number of linkages. The average interevent distance was found to be ~550 m. The HypoDD results are shown in map view and along two mutually perpendicular cross sections in Figure 3. The diffused seismicity seen in Figure 2 is now sharp with a reduced number (118) of very well located events. The uncertainty of location with respect to the cluster center is within a few hundreds of meters for most of the events except a very few small earthquakes ($M_L \leq 2.0$), especially in the SW cluster, whose uncertainty values reaches ~1 km. To further test the errors in relative location with respect to cluster center, bootstrapping was done in which the HypoDD relocation was repeated by replacing stations one at a time. The average error variance was found to be ~5%. The seismicity appear as two distinct clusters of different depth range parallel to the local deformation front and separated by a distance of ~22 km. The NE cluster is close to the Kishtwar Window with focal depth ranging from 13 to 18 km while the SW cluster is shallow with a depth range of ~4 – 15 km. Seismicity at a depth of ~7 – 15 km in the SW cluster is obvious, but earthquakes shallower than 7 km (see cross-section B1 – B1′ of Figure 3) is unanticipated and seems implausi-

ble given the fact that active fault fronts (MFT and MBT) are much farther to the south. However, cross-section B2–B2′ shows us that the seismicity shallows gradually toward the NW from SE and not vertically up. We will see later that this shallow seismicity is an effect of the local structure as well as of the distinct tectonics in this region. The number of large earthquakes ($M_L \geq 3.0$) are more in the NE cluster compared to the SW cluster, which is expected as they are produced in the vicinity of the locked zone of the MHT. The magnitude histogram is shown in the inset of Figure 3.

4. Earthquake Source Mechanism

In order to gain more insights into the style of deformation in this region, we computed the source mechanisms of the larger events. Among the best located events (by HypoDD), we find 21 earthquakes with $M_L \geq 3.0$. Global data from GDSN stations were available for computing source mechanisms for the two largest events (M_L 5.0 and M_L 4.8), whereas for the rest of the events, we used local data from our network of stations.

4.1. Source Mechanism Using Global Teleseismic Data

We used the moment tensor inversion algorithm of McCaffrey and Abers (1988) to calculate the source mechanism of the two largest events. In this method, the broadband teleseismic (30° ≤ epicentral distance ≤ 80°) waveform from 49 GDSN stations were converted into long-period waveforms, first, by removing their respective instrument responses and then by adding the response of long-period (15–100 s) WWSSN (World-Wide Standard Seismographic Network) instruments. *P* and *SH* waveform windows (60 s, starting 2 s before the theoretical time mark) cut from the vertical and tangential component seismogram, respectively, are inverted. Synthetics were computed for a point source within a simple Earth structure by convolving the source time function with the Green's function computed for direct, reflected, and multiple phases. We considered a two-layer velocity model with the first layer being an average of the first 10 km of the velocity model given in Table 1 and the second layer a half-space. The source was assumed to be in the second layer. The source time function was defined to be made up of multiple overlapped isosceles triangles of 1.5-s half-width. The misfit between the observed and synthetic *P* and *SH* waveforms (40-s windows) were minimized in the least square sense, iteratively and the minimum misfit solution is chosen as the final result. In our analysis, we assumed the isotropic component to be zero and the source mechanism was computed for a double couple solution. Details of the methodology can be found in McCaffrey and Nabelek (1987) and Nabelek (1984). We found both the earthquakes to have undergone thrust motion with moderate dips and centroid depths of 15 and 16 km, respectively (Table 2). The best solution for the M_L 4.8 earthquake for both *P* and *SH* waveforms is shown in Figure 4a along with the match between the observed (solid) and synthetic (dashed) seismograms and the resultant source time function. Among the two nodal planes, we chose the NE dipping plane as the fault plane, as it matches with the geometry of the known thrust fault system in the Himalayas; however the dips are slightly steeper than usually observed. The strike, dip, and rake for the preferred fault plane of the M_L 4.8 earthquake is 346°, 49°, and 146° (shown in the header of Figure 4a) while that of the M_L 5.0 earthquake is 326°, 42°, and 110°, respectively. They both strike NW-SE, similar to the strike of the underthrusting Indian Plate in this region. A minor strike-slip component is also observed in the rake of the M_L4.8 earthquake. The scalar seismic moments for both the earthquakes were of the order of 10^{17} Nm.

Evenly distributed azimuthal coverage of stations for the *P* waveform provides a tight constraint to the best fitting solution and the near-source surface reflections constrain the depth of the earthquake. To further examine trade-offs, we performed tests for depth, strike, dip, and rake. In these tests, the tested parameter is fixed within certain interval of the best solution and the inversion is performed with all other parameters free to vary. The tests for M_L 4.8 earthquake for depth, strike, dip, and rake are shown in Figures 4b–4e, respectively. We can see that there is no significant change in the modeled strike, dip, and rake with variation in depth (Figure 4b). The minimum change in misfit value (36–41 R/D%) is chosen as the 1σ deviation from the mean depth. Here we get a depth variation of 16 ± 4 km. However, probabilistic and relative locations (sections 3.2 and 3.3) showed the uncertainty of depth within ~1.5 km, also long-period signals used in this methodology cannot resolve depths smaller than 5 km. Therefore, we stick to the depth uncertainty from our location results. Similar results were also obtained for the M_L 5.0 earthquake. Tests for strike and dip showed normal distribution of the misfit value and the 1σ variation was calculated as 6° and 8°, respectively. For rake, the misfit distribution was slightly skewed and the variation is computed as $1\sigma = \frac{1}{2}(Q3 - Q1)$, where $Q1$ and

Geochemistry, Geophysics, Geosystems

10.1029/2018GC007597

Table 2
Table Showing the Source Mechanism Results

No.	Origin time (UTC) (dd/mm/ear hr:min:s)	Latitude (°N)	Longitude (°E)	Depth (km)	Magnitude	Fault plane Strike (°)	Fault plane Dip (°)	Fault plane Rake (°)	Auxilliary plane Strike (°)	Auxilliary plane Dip (°)	Auxilliary plane Rake (°)	Remarks
1	23/8/1980 21:36:55.2	32.9637	75.7509	15.0	5.5	293	10	63	140	81	95	Global CMT
2	23/8/1980 21:50:05.7	32.9023	75.7974	15.0	5.5	298	12	82	126	78	92	Global CMT
3	1/5/2013 06:57:17.9	33.0600	75.8200	16.0	5.6	346	26	121	124	69	81	Mitra et al. (2014)
4	8/2/2013 21:37:40.4	33.2508	75.8488	15.6	5.0	326 ± 6	42 ± 4	110 ± 6	120 ± 6	51 ± 4	73 ± 6	This study (global data)
5	8/2/2013 02:32:45.9	33.2401	75.9242	16.1	4.8	346 ± 8	49 ± 6	146 ± 9	100 ± 8	65 ± 6	46 ± 9	This study (global data)
6	8/18/2013 23:53:27.0	33.2925	75.7522	13.5	4.2	283 ± 3	32 ± 2	58 ± 5	139 ± 4	64 ± 2	108 ± 3	This study (local data)
7	7/30/2013 18:09:22.6	33.1110	75.6857	13.2	4.0	35 ± 7	9 ± 3	−122 ± 4	247 ± 3	83 ± 3	−85 ± 3	This study (local data)
8	7/22/2013 09:07:25.6	33.1123	75.6765	12.1	3.9	166 ± 5	24 ± 2	140 ± 4	294 ± 4	75 ± 2	71 ± 4	This study (local data)
9	8/19/2013 03:18:43.2	33.1793	75.6201	9.2	3.8	48 ± 9	3 ± 4	−165 ± 10	303 ± 5	88 ± 2	−84 ± 6	This study (local data)
10	8/14/2013 07:37:31.6	33.2454	75.7963	15.2	3.8	287 ± 4	27 ± 2	16 ± 4	183 ± 3	83 ± 2	116 ± 2	This study (local data)
11	8/5/2013 13:57:43.2	33.2047	75.8758	14.3	3.8	265 ± 7	3 ± 2	83 ± 3	92 ± 4	83 ± 2	91 ± 3	This study (local data)
12	8/3/2013 09:31:05.4	33.2447	75.8374	17.3	3.8	279 ± 1	55 ± 3	5 ± 4	186 ± 4	86 ± 3	145 ± 4	This study (local data)
13	8/2/2013 22:42:01.2	33.2723	75.8006	15.8	3.8	316 ± 4	50 ± 1	109 ± 4	108 ± 5	43 ± 1	69 ± 4	This study (local data)
14	8/19/2013 01:10:28.1	33.3061	75.7340	13.5	3.7	278 ± 9	29 ± 1	104 ± 4	82 ± 6	62 ± 2	82 ± 3	This study (local data)
15	8/4/2013 20:38:39.7	33.1691	75.6536	10.5	3.5	22 ± 1	48 ± 2	−146 ± 2	268 ± 4	65 ± 2	−47 ± 2	This study (local data)
16	8/29/2013 06:18:19.3	33.1933	75.5991	7.7	3.4	343±8	18±1	-66±3	138±5	73±1	-98±2	This study (local data)
17	8/2/2013 02:40:50.8	33.2534	75.8040	13.2	3.3	244 ± 9	22 ± 2	110 ± 2	42 ± 4	69 ± 4	82 ± 3	This study (local data)
18	9/1/2013 02:33:56.9	33.1432	75.6549	11.6	3.2	34 ± 4	30 ± 3	−134 ± 2	263 ± 3	69 ± 2	−68 ± 2	This study (local data)
19	8/4/2013 04:34:45.8	33.2956	75.7571	14.1	3.2	356 ± 6	86 ± 1	−106 ± 2	252 ± 5	17 ± 3	−15 ± 2	This study (local data)
20	8/2/2013 18:49:41.1	33.2546	75.8492	18.5	3.2	283 ± 2	56 ± 1	39 ± 4	169 ± 2	59 ± 1	139 ± 3	This study (local data)
21	8/7/2013 21:21:35.8	33.2869	75.7877	14.1	3.1	289 ± 3	33 ± 4	9 ± 5	192 ± 2	85 ± 2	122 ± 4	This study (local data)
22	8/5/2013 15:38:30.6	33.2640	75.7753	13.2	3.1	276 ± 3	65 ± 2	55 ± 4	154 ± 4	42 ± 3	141 ± 4	This study (local data)
23	8/29/2013 16:33:32.3	33.2124	75.8852	18.3	3.0	295 ± 5	39 ± 3	−6 ± 4	29 ± 2	86 ± 3	−129 ± 4	This study (local data)
24	8/2/2013 19:42:47.1	33.2295	75.8053	15.9	3.0	265 ± 10	45 ± 4	8 ± 8	169 ± 10	84 ± 4	135 ± 9	This study (local data)

Note. The first three mechanisms are of past events in this region, while the rest are computed in this study. They are sorted according to magnitude. The uncertainties in strike, dip, and rake are mentioned. Beach ball representation of these results are shown in Figure 6.

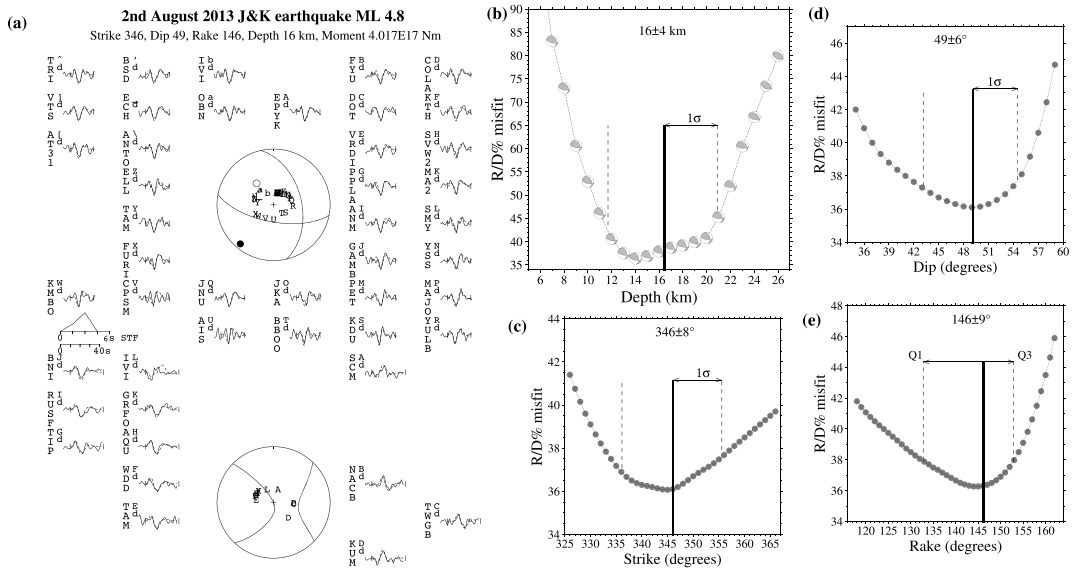

Figure 4. (a) *P* (top) and SH (bottom) focal mechanism and waveforms (observed = bold, synthetic = dashed) for the minimum-misfit solution of the M_L 4.8 earthquake (Table 2) is shown. The short time function was found to be of half width ∼2.9 s. The station position is represented in the focal sphere by a letter indicated between the waveform and the station code. The time window used for the inversion is marked by vertical lines on each waveform. The best fitting focal parameters are written on the top of the plot. (b) The depth sensitivity plot is shown. Depths were fixed at every 1 km between 7 and 26 km, allowing all the other parameters to vary freely. The minimum misfit is obtained for a focal depth of 16 km with 1σ deviation of 4 km. Plot of the uncertainty estimation of (c) strike and (d) dip. The minimum misfit value for strike is found to be 346° and that for dip is 49°. The 1σ deviation for strike and dip are 6° and 8°, respectively. (e) The uncertainty estimation of rake is shown. It is seen to have a skewed distribution and therefore the spread is calculated using first quartile (Q1) and third quartile (Q3). The best estimated value is 146° ± 9°.

*Q*3 represent the first and third quartiles of the data. The deviation for rake was found to be 9°. One σ deviation for the strike, dip, and rake of M_L 5.0 earthquake was also computed in a similar way, and the results are stated in Table 2.

4.2. Source Mechanism of Events Smaller than M_L 4.5

To find the source mechanism using local broadband data, we used ISOLA (ISOLated Asperities), a Fortran-based moment tensor retrieval software package (Sokos & Zahradnik, 2008, 2013). It employs the theory and methodology similar to Kikuchi and Kanamori (1991) but on full waveforms instead of just teleseismic *P* waves and, hence this method could be applied to local and regional events. In this method, the source is assumed to be made up of a sequence of point sources of various focal mechanisms. The synthetic seismograms are approximated by the linear combination of far-field source time functions (STF) and six elementary moment tensors. The coefficients of these linear combinations represent the solution set and is obtained by iterative deconvolution algorithm. Iterative deconvolution involves updating the synthetic seismogram iteratively by varying the number of STFs and/or varying the scalar coefficient values, simultaneously calculating the correlation between the observed and the synthetic seismogram. The iteration is stopped when there is no significant increase in the correlation value any more. For theory, see Kikuchi and Kanamori (1982) and Kikuchi and Kanamori (1991).

At first, displacement records were obtained by removing instrument response from each seismogram and integrating. The records were band-pass filtered within a range of 0.01 – 2 Hz. The high frequencies are limited due to scattering as well as realistic modeling of the waveforms, while the extremely low frequencies do not provide sufficient polarity information. The crustal model was defined by the velocity structure of four nearest stations (joint inversion results from Sharma et al., 2018, for BADR, PHAG, SMVD, and UDHM) and that of the intervening region and other stations (the average velocity model is given in Table 1). The number of velocity models is limited by the program. Several trial sources were defined below the epicenter along with the catalog focal depth to test the correlation (between the observed and synthetic waveforms) with depth. Each of the sources is assumed to be made up of triangular moment rate functions of half-width 0.8 – 1.5 s, depending on the magnitude of the event. Synthetics were generated for each trial source, and the inversion

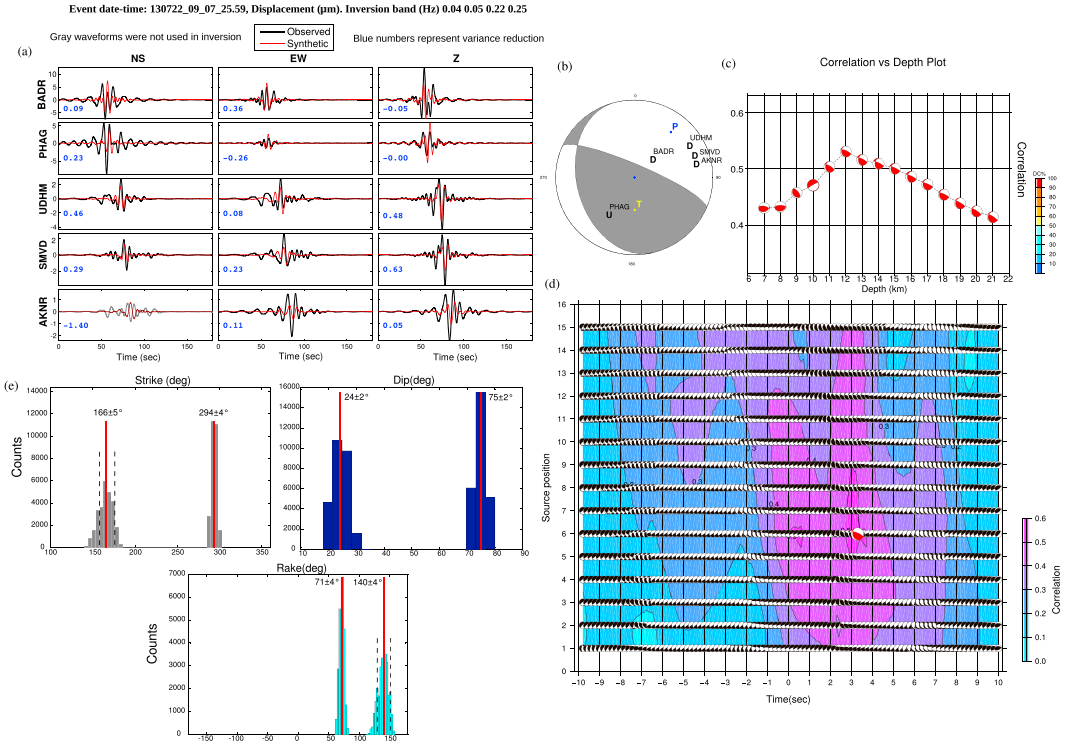

Figure 5. Inversion results for the M_L 3.9 earthquake (Table 2) using ISOLA. (a) The correlation between the observed (black) and synthetic (red) waveforms for all the components of all the stations are shown. Waveforms indicated by gray were not used in inversion. Variance reduction is indicated in blue. The frequency range used for this earthquake is 0.04–0.25 Hz and is shown on the top of the figure. (b) The source mechanism in beachball representation is shown. The polarities of the stations are indicated as U (up) and D (down) motion within the focal sphere. The pressure (*P*) and tension (*T*) axes are also indicated. (c) The plot of correlation with depth is shown. Maximum correlation is obtained for a focal depth of 12 km. Since the inversion is done for strict double couple, we see 100% DC of the beach balls. (d) A plot between the source time shift and source number is plotted along with correlation contours. The color scale of the correlation values are shown on the right. We see that the maximum correlation is obtained for a source time shift of ~3.5 s. The resultant beachball is increased in size and shown as red. (e) The numerically calculated histogram of strike, dip, and rake are shown in different colors. The 1σ width is marked by black dashed lines (see strike and rake) for histograms with larger spread. In other cases, the whole histogram is assumed to be of width 1σ. ISOLA = ISO-lated asperities.

was done for a strict double-couple solution as the station distribution is unfavorable for a full moment tensor inversion. The inversion result for an M_L 3.9 earthquake is shown in Figure 5. Figure 5a shows the match between the observed (black) and synthetic (red) seismograms for all the components of the representative stations. The N-S component of the station AKNR was not used in the inversion as it was too noisy. It is shown as gray in the figure. The variance reduction for each seismogram is shown as blue numerals. The higher the absolute value, the better the correlation is. Figure 5b shows the source mechanism in beachball representation and the polarities of the stations (U for up and D for down motion) are indicated. Figure 5c shows the correlation with depth variation. We see that the correlation is highest for a depth of 12 km. Source time shift is the difference between the moment rate function center time and the rupture nucleation time. The plot between the source time shift and source number is shown in Figure 5d. The source mechanism at each grid point is shown against correlation contours (color scale). The maximum correlated solution is obtained for a source time shift of ~3.5 s, and the resultant beach ball is shown in red. ISOLA allows for the numerical construction of an error ellipsoid by regularly sampling the parameter space around the best solution (Sokos & Zahradnik, 2013). From the error ellipsoid, a statistical set of strike, dip, and rake are obtained whose histograms can be constructed. Figure 5e shows such histograms for strike, dip, and rake of the M_L 3.9 earthquake. The thick red line represents the optimal solution. The width of the 1σ deviation is indicated by dashed line (see strike and rake) when the spread is large; otherwise the whole distribution is assumed 1σ. The strike, dip and rake of the two nodal planes are found to be 294 ± 4°, 75 ± 2°, 71 ± 4°, and 166 ± 5°, 24 ± 2°, 140 ± 4°, respectively. Similarly, the source mechanism and their uncertainties for all the other earthquakes were also

computed and are tabulated in Table 1. The source mechanisms of all the 21 computed events are shown in Figure 6 in the map and two cross sections (B1–B1′ and B2–B2′) along with the mechanisms of some older events. The mechanisms calculated using global data are shown in green, mechanisms using local data in orange and that of older events (1980 and May 2013) in magenta. Source mechanism of all the earthquakes in the NE cluster shows dominant thrust motions with the dip direction toward NE or N-NE. However, the focal mechanisms of most of the events in the SW cluster are dominantly normal, which is very uncommon in a thrust regime. The details of this observation and the implications of all the results are discussed next.

5. Discussion

5.1. Local Ramp Structures on the Underthrusting Indian Plate between MCT and Kishtwar Window

Our analysis shows the recent seismic activity in the region between the MCT and Kishtwar Window (Figure 3). The activity reveals itself in two distinct earthquake clusters separated by a distance of ∼22 km. The clusters align parallel to the strike of the underthrusting plate in the western syntaxis (NW-SE strike) but at different depths. The NE cluster concentrates at a greater depth than the other and is very close to the Kishtwar Window. The southern and eastern part of the Kishtwar Window coincides with the 3.5-km elevation contour (dashed red line in Figure 2). The 3.5-km elevation contour is identified as a proxy to the locking line in the central Himalaya, north of which the Indian Plate creeps aseismically at depths below ∼18 km (Bollinger et al., 2004). We observe that the earthquakes (in the NE cluster), which are in the periphery of the 3.5-km elevation contour lie at depths of ∼15–18 km while those away from it are shallower (13–14 km) (Figure 6). We do not see any earthquakes farther to the northeast, which implies that these deep earthquakes (depth 15–18 km) mark the locking line in the Kishtwar Window. The largest earthquakes in our analysis (M_L 5.0 and 4.8) also lie in this region. The rapid change in depth of the events from ∼13 to ∼16 km might indicate the presence of a steep frontal ramp just west of the Kishtwar Window. To test this, we plotted the strike and dip directions of the fault planes of all the earthquakes analyzed in this study using geological map symbols (Figure 7a). The line segments showing dip direction were scaled by the dip amount. The judgment of the fault plane is made on the basis of dip direction. The nodal plane whose dip direction had an east component (similar to the dip direction of the known thrust sheets—MCT, MBT, etc.) was chosen. It is seen that the dips of the deeper events (close to the Kishtwar Window trace) were greater than those of the shallower events. Taking depth of all the events and considering dip, we made depth contours (Figure 7a). From the contour plot (NE cluster region), we see that the depth increases from 13 to 18 km over a distance of ∼12 km, which gives a localized dip of ∼22°. We plotted the apparent dips of the events (not true dips because the strike of the events and cross section vary) in both the cross-sections B1–B1′ and B2–B2′, respectively (Figures 7b and 7c). A trace through the apparent dips in the cross-section B1–B1′ (Figure 7b, green dashed line) highlights the steep dip. In Figure 7c, the trace (green) shows a concave-convex surface. To simplify, we made two blocks (in green) dipping to the NE and N-NE (Figure 7d), respectively, as the two convex surfaces and a gap representing the concave surface. These two blocks (exaggerated in dimension) represents a steep frontal ramp model in the Kishtwar Window region and is able to explain our observations in terms of dip, dip direction, and seismicity.

The strike and dip direction of the events in the SW cluster seismicity were not as straightforward as the events in the NE cluster. Here five out of six events were found to have undergone normal motion. The fault plane solution for all the earthquakes in this cluster showed two possible orientations: (i) NE-SW striking faults with gentle to moderate dips in the SE direction (Figure 7d) or (ii) East/E-NE striking near-vertical faults (Figure S2 in the supporting information). The presence of normal faults creates a stir initially; however, literature survey reveals that normal faults are not so uncommon in this region. Normal faults like *Oldham's lost fault* have been reported earlier in this region (Bilham et al., 2013; Schiffman et al., 2011), although at very shallow depths. In view of this, we chose the NE-SW striking nodal plane as the fault plane for the time being. We will also discuss the consequences of choosing the other nodal plane as the fault plane later in the text. Depth contours based on the depths and dip of events show contours gradually shallowing in the NW direction. Traces through the apparent dips in cross-section B1–B1′ (Figure 7b, magenta dashed lines) shows an upwarped region at a depth of 8–12 km. Numerous such arch-like traces can be imagined perpendicular to the plane of the cross section (drawn as one on top of the other). The trace (magenta) in cross-section B2–B2′ (Figure 7c) clearly shows an elevated region. Since the depth of the events shallows in the NW direction and the computed source mechanisms show dip in the SE direction, we presume that the earthquakes lie on a SE dipping structure. The simplest block diagram that can represent our observations is a wedge or lateral ramp dipping in the SE direction with a flat portion on the top (shown in magenta in Figure 7d). The flat portion is drawn to take

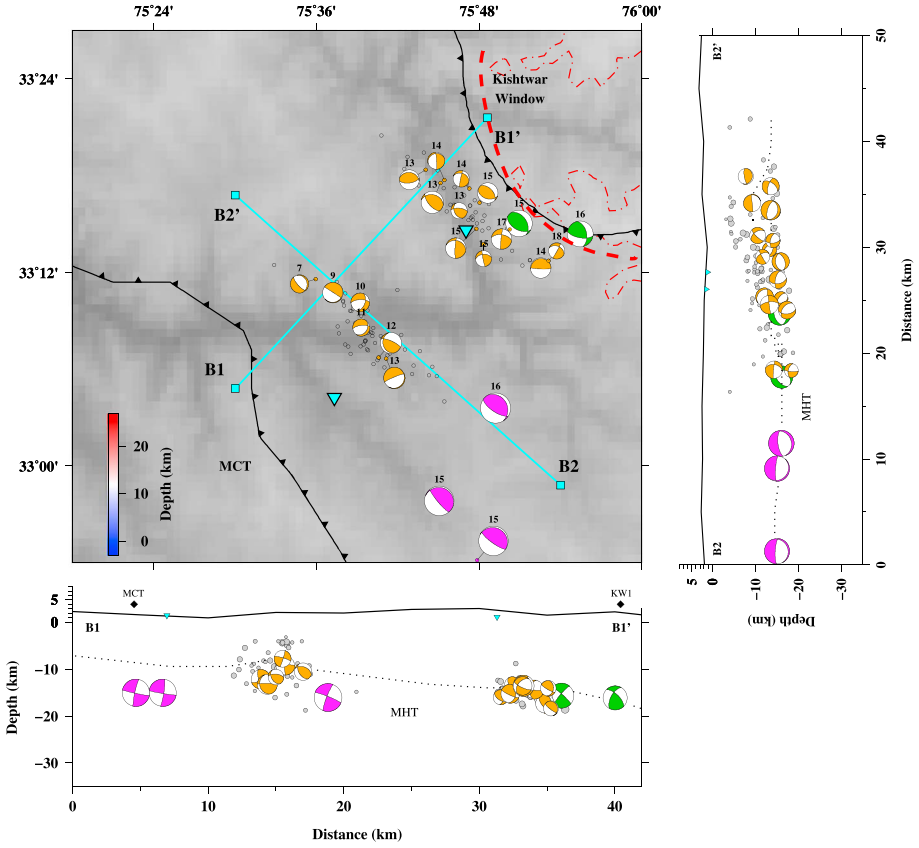

Figure 6. Plot of source mechanisms, as beachballs, of all the earthquakes used in this study in map view and cross sections along two profiles B1–B1′ and B2–B2′ perpendicular and parallel to the deformation front, respectively. The depths of the event are indicated above the beachball in map view. The remaining microseismicity is plotted in the background as circles (black in map, gray in cross sections). The source mechanisms shown in magenta correspond to two 1980 M_W 5.5 events (GCMT solutions, reviewed ISC location) and May 2013 M_W 5.6 earthquakes (Mitra et al., 2014). The source mechanisms obtained by global data ($M_L \geq 4.5$) are shown as green while that using local data (M_L <4.5 are shown in orange. The cyan triangles represent stations. The actual 3.5-km elevation contours are shown by thin dash-dotted lines (red). The representative 3.5 elevation contour is approximated from the actual contours and is represented by thick red dashed line. Approximated topography of the Main Himalayan Thrust is shown as dotted lines in the cross sections. The known geological features—Main Central Thrust and Kishtwar Window (KW1)—are indicated on the cross-section B1–B1′ as diamonds (blue)

into account the fact that depth of some of the events increases in this part. The lateral ramp lie between the Kishtwar Window and MCT at a depth of 7–13 km and has an average dip of 13°. This lateral ramp structure can also explain the presence of normal faults if extension occurs along the ramp in the SE direction. The dip of the 2013 Kishtwar event was also found to be steeper than usual (Mitra et al., 2014). This could indicate the presence of more lateral ramp-like structures to the SE of our observation.

If the two local structures are joined in the simplest way, we see two bulge structures connected by a flat (dotted line in Figure 7b). Geological studies on the Kishtwar Window and its vicinity (Singh, 2010; Thakur, 1998), often show a reclined S-shaped topography of the overlying thrust sheets (MCT, Kishtwar thrust, etc.) similar to what we have found here, but at much shallower depths. Joint inversion of receiver function and surface wave dispersion study in this region (Sharma et al., 2018) shows the MHT at 10–14 km for station BADR and 14–16 km in PHAG. These two stations are closest to the SW cluster and the NE cluster, respectively. West of our study region, the MHT is found at depths of 8–10 km (SMVD). Another joint inversion of receiver function and dispersion study (Mir et al., 2017) in the Kashmir Basin (NW of the Kishtwar Window) shows the MHT at ~15 km. Therefore, we can infer that all the earthquakes of the NE cluster and the earthquakes lying at a depth of 8–13 km in the SW cluster occurred on the MHT and not on the overlying thrust sheets and that the MHT topography has two elevated structures. It also implies that the S-shaped topography of the MCT and the other thrust faults reported in the geological studies in this region are influenced by the

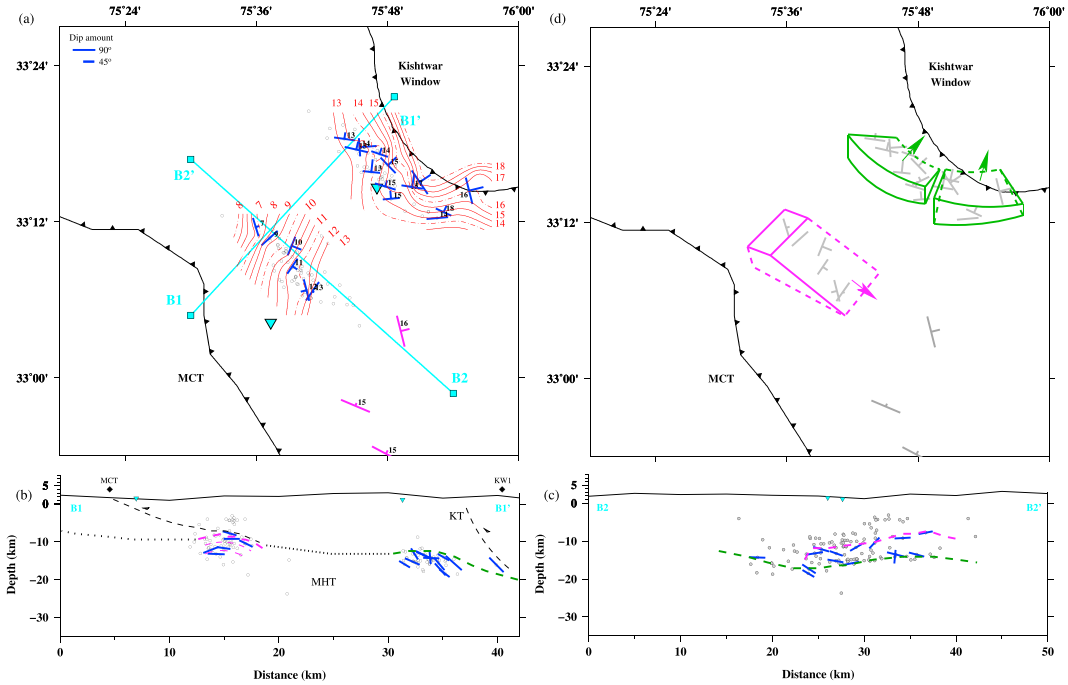

Figure 7. (a) Plot of the strikes and dips of the preferred fault planes of all the earthquakes used in this study in map view. The strike and dip of 1980 and May 2013 events are drawn in magenta while that of other events in blue. The depths of the events are shown adjacent to them. Profiles B1–B1′ and B2–B2′ are drawn as cyan lines and stations as cyan triangles. The background seismicity is shown as circles. Contours are drawn in red based on the depth of the bigger events, their dips, and the depth of the background microseismicity. (b) The apparent dips of the events on cross-section B1–B1′ are shown in blue. The traces through the apparent dips of the events in NE cluster is shown by green dashed line, while that for events in the SW cluster is shown by magenta dashed line. The dotted trace joins the two local structures in the simplest possible way. The inferred Main Central Thrust and Kishtwar thrust (KT) traces are shown as black dashed line and are partially inspired from Singh (2010). (c) The apparent dips of the events on cross-section B2–B2′ is shown in blue. The envelope through the apparent dips of the events in NE and SW clusters are shown in green and magenta, respectively. (d) Block diagrams representing the inferred geometry are drawn in map view with slight vertical exaggeration. The structure close to NE cluster is shown in green while that close to SW cluster is in magenta. The arrow heads indicate dip direction of the blocks. The strike and dip of the individual events are shown in gray.

topography of the MHT. Upwarping of the overlying thrusts due to the MHT structure were also reported in Sikkim (Paul & Mitra, 2017). Two relevant observations from the Sikkim Himalaya regarding the dome-shaped (or elevated) structures on the MHT are as follows: (i) they can give rise to a network of fractures and hence microseismicity in the region overlying them, and (ii) they can make the overlying thrust sheets wrap around them resulting in an arcuate surface expression (Paul & Mitra, 2017). Similar observations are seen here as well. We see microseismicity lying at a depth of ~4–7 km just above the flat portion of the ramp structure (in the SW cluster). The MCT just west of this elevated structure has greater curvature compared to its adjacent parts (Figures 7a and 7d). We also see normal faulting perpendicular to the deformation front, which is difficult to explain in the absence of a lateral ramp. These evidences strongly validate the existence of lateral ramp. The steep dip of the Kishtwar thrust (as reported in Singh, 2010) compares well with the steep ramp of the MHT beneath the NE cluster of events, while the gentler dip of MCT (Singh, 2010) is similar to the gentle dip of MHT beneath the SW cluster of events. These coincidences can be associated with the splaying of the Kishtwar thrust and the MCT from the MHT at these two regions.

5.2. Importance of Lateral Heterogeneities and Their Implications in the Southeastern Jammu and Kashmir Himalaya

Bilham et al. (2013) and Schiffman et al. (2011) reported normal faults in the SE edge of Kashmir Valley (33.56°N, 75.51°E) ~30 km NW of the location of the M_L 4.0 normal fault earthquake in this study. These normal faults were originally identified by Oldham in the year 1881 and were referred to as *Oldham's lost faults* on their rediscovery (Bilham et al., 2013). The rediscovered normal faults lie within a few kilometers of the surface,

while the normal faults computed in this study lie at a depth of ~7–13 km and hence the two could not be linked. However, we did find numerous similarities between the two. Bilham et al. (2013) and Schiffman et al. (2011) noted that these near-surface faults could have been caused by bulge/flexure along an east-southeast axis on the Indian Plate. Interestingly, the lateral ramp/elevated structure interpreted in this study also dips in the southeast direction (Figure 7) and the surface normal faults (which are located to the northwest of the deep normal faults) align exactly updip of the lateral ramp structure. Bilham et al. (2013) and Schiffman et al. (2011) also reported the presence of five faults with 5-km spacings south-southeast of the Oldham's lost fault. All these faults seem to follow the dip of the ramp structure. The shallow normal faults are probably caused by gravity collapse in the mountains (top of the hanging wall and the wedge, Bilham et al., 2013). Similarly, we can argue that such gravity collapse can occur within or at the bottom of the hanging wall along the ramp structure present on the foot wall surface. This is also in accordance with the fact that the geometry of the shallow structures often closely resemble the geometry of the MHT zone. The normal fault earthquakes (this study) detected within the vicinity of the MHT could have been caused by this process. Schiffman et al. (2013) pointed out folding near Riasi, which are also associated with underthrusting bulge structure; however, the reported bulge is at a distance of ~50 km NW of our modeled lateral ramp (Figure 2 in Schiffman et al., 2013). This result implies the presence of more lateral/elevated structures in this region. The lateral ramp or the elevated structure found here can be regarded as a lateral heterogeneity on the underthrusting Indian Plate within a crustal shortening regime. Similar lateral heterogeneity in the form of lateral ramp was also suggested on the MHT beneath Kangra recess and Nahan salient (Rajendra Prasad et al., 2011). This region is ~150 km southeast of our study region and almost coincides with the SE edge of the 1905 Kangra rupture zone (Figure 1). Rajendra Prasad et al. (2011) hinted this lateral ramp terminating the 1905 Kangra earthquake rupture as one possibility. The capability of lateral heterogeneities terminating rupture propagation were discussed in detail for subduction scenarios in Wang and Bilek (2011) and its applicability to the MHT in the Sikkim Himalaya in Paul and Mitra (2017). The magnitude and location of the 1555 earthquake was only based on six felt reports, and hence, its dimensions of rupture are only approximate, yet we can say that the bulge structures reported by Schiffman et al. (2013) exist to the SE of the rupture edge. If that is the case, it is possible that the lateral rupture propagation of the 1555 earthquake could have been curtailed by these lateral heterogeneities. A plot of the seismicity in the last 100 years shows large concentration of shallow seismicity coinciding with the NW edge of the 1905 Kangra rupture zone (Figure 1). Also, the aftershocks of the 1905 Kangra earthquake occurred southeast of the mainshock (Szeliga & Bilham, 2017) only. It might again indicate the presence of more lateral heterogeneities in the NW edge of the 1905 Kangra earthquake rupture, which prevented aftershocks in this direction. However, this supposition needs to be backed-up by more concrete evidence before anything conclusive can be suggested. We could see how the edges of the rupture zone of the 1905 Kangra earthquake and the possible rupture zone of 1555 earthquake coincided with the presence of lateral heterogeneities (like lateral ramps, elevated structures, or shallow seismicity). A few possible scenarios evolve out of these evidences regarding the megathrust earthquakes—(i) rupture initiating at smooth surfaces (absence of heterogeneities) are not able to propagate beyond these lateral heterogeneities resulting in less-than-expected slip and magnitude, (ii) weak coupling between the footwall and hanging wall (lateral heterogeneities like elevated structures on the footwall creates a network of fractures or creep zone on the hanging wall (Wang & Bilek, 2011)) lessens stress buildup, and/or (iii) if sufficient amount of stress is accumulated in the smooth region without slipping over a longer period of time, it might be able to break past these heterogeneities resulting in a very great earthquake as estimated in Schiffman et al. (2013). The slip deficit of ~14 mm/year observed in the NW Himalaya (Banerjee & Bürgmann, 2002) could be partially due to the first scenario. The interseismic coupling results using GPS geodesy (Stevens & Avouac, 2015) show lack of coupling in the region where we and others (Rajendra Prasad et al., 2011; Schiffman et al., 2013) have located the heterogeneities but intense coupling at the edges which supports our second scenario. The longer duration of quiescence since the 1555 earthquake might also indicate accumulation of more slip according to our third scenario. The absence of great earthquakes in the SE Kashmir and the Jammu Himalaya might be a consequence of these heterogeneities; however, it also opens up the possibility of greater-than-expected great earthquakes in the region when sufficient stress is accumulated.

5.3. Structural Control, Strike Slip Component, and Possible Causes of the SW Cluster of Seismicity

The greatest earthquake in the north Kashmir and Hazara Syntaxis manifested in 2005 as a M_W 7.6 earthquake. The 2005 Kashmir earthquake did not occur on the MHT but on a steep splay fault, and it was demonstrated to be an out-of-sequence thrust earthquake (Avouac et al., 2006). Kaneda et al. (2008) also affirmed that

neither the MBT nor the MFT took part in the 2005 Kashmir earthquake but an intervening fault called the Bagh-Balakot fault. The fault rupture of the 2005 Kashmir earthquake terminated abruptly in the hairpin corner of the Hazara Syntaxis (Avouac et al., 2006) but stresses continued to release in a blind wedge thrust beneath the IKSZ (Bendick et al., 2007). It demonstrates the strong structural control on fault rupture in the western syntaxis. Similarly, NW of the Kishtwar thrust (i.e., in the direction of updip of the deformation front), the presence of lateral heterogeneities influence strong structural control. In terms of slip, the dominant regime in the western syntaxis is NE-SW shortening (Banerjee & Bürgmann, 2002; Bendick et al., 2007) instead of right-lateral shear, which is expected in the syntaxes due to crustal extrusion. The slip of the 1905 Kangra earthquake was also mainly reverse, but a small percentage of strike-slip component was computed for various location of the estimated fault endpoint (Wallace et al., 2005). By geologic mapping and paleoseismic studies, Malik et al. (2015) identified an active dextral strike-slip fault in the Kangra Valley (and named it as Kangra Valley Fault) and inferred it to be the surface rupture of the 1905 Kangra earthquake. However, Szeliga and Bilham (2017) estimated only 0.6 m of dextral slip on the Kangra Valley Fault (KVF), if at all it slipped, which could contribute only about 2% of the total moment released in the 1905 Kangra earthquake. On the contrary, they found good probability for the presence of a dextral component to the dip slip along MHT. The source mechanism computed in our study also showed the presence of minor strike-slip component for a few dip slip events along the MHT. The 1905 Kangra earthquake might not have occurred on the KVF, nonetheless KVF is identified as an active 60-km strike-slip fault known to have slipped most recently post 1620 (Malik et al., 2015). Additionally, at least three moderate earthquakes in the year 1968, 1978, and 1986 occurred at a depth range of ~10–15 km in the Kangra Valley (Kumar & Mahajan, 2001) and they showed prominent strike-slip components to dip slip along the MHT. These earthquakes had nodal planes striking transverse to the Himalayan trend very similar to some of the events computed in this study. All these evidences indicate the existence of strike-slip motion, however small, in the Kangra reentrant and Kishtwar window.

The observed SW cluster of seismicity appears ~22 km southwest and updip of the seismicity in the main crustal ramp (locked zone). This phenomenon is unusual where stresses seem to propagate updip skipping an extended region. It also raises the question whether the flat decollement between the two seismicity clusters is creeping. Neither do we see any seismicity (neither in the plot of the events from each step of our location analysis nor in the plot of historical seismicity from 1905 to 2013) in the region between the two clusters, nor do the pressure-temperature condition at these depths (~10–13 km) or the elevation contours above this region supports creeping. Creeping of the horizontal fault due to the existence of extremely high fluid pressure on the decollement can also be disproved as we do not see any extremely low velocity zones at these depths from joint inversion studies (Sharma et al., 2018; Mir et al., 2017). On the contrary, there is sufficient evidence of the existence of lateral heterogenities trending transversely to the strike of the Himalaya (deformation front) as well as the existence of a small amount of strike-slip component to dip slip in these regions. We believe that the seismicity in the SW cluster is probably a resultant of the strike-slip component (both dextral and sinistral) of the plate motion loading/unloading stresses on the lateral heterogeneities within the underthrusting plate. On the other hand, if we assume the east striking nodal plane as the fault plane, a simplistic block diagram (Figure S2 in the supporting information) indicate offsets between vertical blocks. This shows extension parallel to the crustal shortening and is very unlikely. We also tested the possibility of reservoir-induced seismicity. We found that the active dams over Chenab (Figure S3 in the supporting information) are far away from the SW cluster of seismicity. The Ratle dam which would be closest (~15 km to the east) to the SW seismicity cluster is not operational yet. Chenab is a huge erosional valley and its location coincides with the SW cluster of seismicity. Unloading of the sediment mass would lead to release of potential energy, and hence, faulting or reactivation of faults could occur. We found that the sediment yield of Chenab is highest during the Monsoon (July–September) and yields about 438.7 t/km^2 of sediment at an average during this period in Premnagar (a region closest to SW seismicity cluster; Rao et al., 1996). A monthly histogram shows the seismicity in the SW cluster peaking during this period (August–October;Figure S4 in the supporting information), which might indicate a causal relationship between the two. The potential energy transfer due to erosion might also favor the occurrence of normal faults by gravity collapse mechanism. From these analyses, we found two possible causes of the SW cluster of seismicity — strike-slip motion loading/unloading stresses on the lateral heterogeneities or gravity collapse backed by potential energy transfer due to sediment loading/unloading on the river Chenab. However, our analysis is unable to pinpoint the actual cause among the two at this moment and this will need further detailed research.

6. Conclusions

The recent seismic activity in the southeastern edge of the Kashmir seismic gap revealed a steep frontal ramp near the locked portion of the MHT and lateral heterogeneities in the form of lateral ramp and elevated structure (NW of lateral ramp) on the underthrusting Indian Plate. The steep frontal ramp coincides with the steep Kishtwar thrust. Dominant thrust motion and earthquakes as large as M_L 5.0 in this ramp indicate crustal shortening. The lateral ramp structure between the Kishtwar thrust and MCT exhibit the presence of normal faults. The two possible causes inferred from our analysis for the existence of normal faults are—(i) the abundant strike-slip component loading/unloading stresses on the lateral heterogeneities or (ii) sediment yield over the river Chenab, transferring potential energy to cause gravity collapse within or bottom of the hanging wall. Elevated structures are known to cause a network of fractures and microseismicity. The very shallow seismicity (4–7 km) in the SW cluster could be due to these network of fractures caused by the elevated flat structure existing northwest of the frontal ramp. The elevated structure mapped in this study and bulged structures from other studies and the associated seismicity extend from at least 76.5°E to 75.5°E longitude, which coincide with the northwestern edge of the 1905 Kangra earthquake and the approximate SE edge of the 1555 earthquake or intervening region of the Kashmir Gap, respectively. These lateral heterogeneities has the potential to create a network of fractures within the hanging wall, which acts as a creep zone for the foot wall to move with ease. This leads to the weak coupling between the footwall and the hanging wall within the region of asperities, but very strong coupling outside of it. We conjecture if a sufficient amount of slip is accumulated within the smooth portion of the MHT, it might be able to break past the asperities giving rise to very great earthquakes. One such smooth region is the meizoseismal zone of the 1555 earthquake with the possibility of its rupture zone extending further SE under high slip accumulation and long quiescence interval.

Acknowledgments

The seismological field experiment was established and operated through multiple grants, viz., UK-India Education and Research Initiative (UK-IERI) Thematic Partnership, 2011–2014 (S. M. and K. F. P.) and University Grants Commission, India,-UK-India Education and Research Initiative (UGC-UK-IERI) Thematic Partnership, 2015–2017 (S. K. W., S. M. and K. F. P.) and Major Research Project from University Grants Commission, India, 2015–2018 (S. K. W. and S.M). H. P. acknowledges Marie-Curie ITN Experienced Researcher fellowship for carrying out this work in the University of Cambridge, UK. S. S. acknowledges the INSPIRE Fellowship (JRF and SRF) from Department of Science and Technology, GoI, D. P. acknowledges the PhD Fellowship from IISER Kolkata, S. M. acknowledges Academic Research Funding (ARF) from IISER Kolkata, S. K. W acknowledges administrative support from SMVDU. Data preprocessing and analyses were performed using Seismic Analysis Code (SAC) (Goldstein et al., 2003). All plots were made using the Generic Mapping Tools version 4.5 (www.soest.hawaii.edu/gmt; Wessel and Smith (1998). The NLloc and HYPODD relocated events are uploaded in the form of spreadsheet(.csv) files as supporting information. The local waveform data used for source mechanism computation is available through the Department of Earth Sciences, University of Cambridge (http://eprints.esc.cam.ac.uk/4255/) in sac format while the global teleseismic waveforms are accessible from IRIS DMC on request (https://ds.iris.edu/ds/nodes/dmc/forms/breqfast-request/). We are grateful to the two reviewers whose constructive reviews and comments have improved the manuscript immensely.

References

Aki, K., & Richards, P. G. (2002). *Quantitive seismology* (2nd ed.). Sausalito, CA: University Science Books.

Ambraseys, N. N., & Douglas, J. (2004). Magnitude calibration of north Indian earthquakes. *Geophysical Journal International*, *159*, 165–206.

Ambraseys, N., & Jackson, D. (2003). A note on the early earthquakes in northern India and southern Tibet. *Current Science India*, *84*(4), 570–582.

Avouac, J.-P., Ayoub, F., Leprince, S., Konca, O., & Helmberger, D. V. (2006). The 2005, M_W 7.6 Kashmir earthquake: Sub-pixel correlation of ASTER images and seismic waveforms analysis. *Earth Planet Science Letters*, *249*, 514–528.

Banerjee, P., & Bürgmann, R. (2002). Convergence across the northwest Himalaya from GPS measurements. *Geophysical Research Letters*, *29*(13), 1652. https://doi.org/10.1029/2002GL015184

Bendick, R., Bilham, R., Khan, M. A., & Khan, S. F. (2007). Slip on an active wedge thrust from geodetic observations of the 8 October 2005 Kashmir earthquake. *Geology*, *35*(3), 267–270.

Bilham, R., Bali, B. S., Ahmad, S., & Schiffman, C. (2013). Oldham's lost fault. *Seismological Research Letters*, *84*, 702–710.

Bilham, R., Gaur, V. K., & Molnar, P. (2001). Himalayan seismic hazard. *Science*, *293*, 1442–1444.

Bilham, R., Larson, K., Freymuller, J., et al. (1997). GPS measurements of present-day convergence across the Nepal Himalaya. *Nature*, *386*, 61–64.

Bilham, R., & Wallace, K. (2005). Future $M_W > 8$ earthquakes in the Himalaya: Implications from the 26 Dec 2004 $M_W = 9.0$ earthquake on India's eastern Plate margin. *Geological Survey of India Special Publication*, *85*, 1–14.

Bollinger, L., Avouac, J. P., Cattin, R., & Pandey, M. R. (2004). Stress buildup in the Himalaya. *Journal of Geophysical Research*, *109*, B11405. https://doi.org/10.1029/2003JB002911

Bormann, P., & Wielandt, E. (2013). Seismic Signals and Noise. In P. Bormann (Ed.), *New manual of seismological observatory practice 2 (NMSOP2)* (pp. 1–62). Deutsches GeoForschungsZentrum GFZ: Postsdam.

Burg, J.-P., Celerier, B., Chaudhry, N. M., Ghazanfar, M., Gnehm, F., & Schnellmann, M. (2005). Fault analysis and paleostress evolution in large strain regions: Methodological and geological discussion of the south-eastern Himalayan fold-and-thrust belt in Pakistan. *Journal of Asian Earth Sciences*, *24*, 445–467.

Drew, J., White, R., Tilmann, F., & Tarasewicz, J. (2013). Coalescence microseismic mapping. *Geophysical Journal International*, *195*(3), 1773–1785.

Goldstein, P., Dodge, D., Firpo, M., & Minner, L. (2003). Sac2000: Signal processing and analysis tools for seismologists and engineers. In W. Lee, H. Kanamori, P. C. Jennings, & C. Kisslinger (Eds.), *The IASPEI international handbook of earthquake and engineering seismology* (Part B, Vol. 81B, 1st Ed). London: Academic Press.

Hutton, L. K., & Boore, D. M. (1987). The M_L scale in Southern California. *Bulletin of the Seismological Society of America*, *77*, 2074–2094.

Iyengar, R. N., Sharma, D., & Siddiqui, J. M. (1999). Earthquake history of India in medieval times. *Indian Journal of History of Science*, *34*(3), 181–237.

Jouanne, F., Mugnier, J., Pandey, M., Gamond, J., Le Fort, P., Serrurier, L., et al. (1999). Oblique convergence in the Himalayas of western Nepal deducedfrom preliminary results of GPS measurements. *Geophysical Research Letters*, *26*(13), 1933–1936.

Kaneda, H., Nakata, T., Tsutsumi, H., Kondo, H., Sugito, N., Awata, Y., et al. (2008). Surface rupture of the 2005 Kashmir, Pakistan, earthquake and its active tectonic implications. *Bulletin of the Seismological Society of America*, *98*(2), 521–557.

Khattri, K. (1999). Probabilities of occurrence of great earthquakes in the Himalaya, Proc. Indian. *Academy of Sciences*, *108*(2), 87–92.

Kikuchi, M., & Kanamori, H. (1982). Inversion of complex body waves. *Bulletin of the Seismological Society of America*, *72*(2), 491–506.

Kikuchi, M., & Kanamori, H. (1991). Inversion of complex body waves III. *Bulletin of the Seismological Society of America*, *81*(6), 2335–2350.

Kumar, S., & Mahajan, A. K. (2001). Seismotectonics of the Kangra region, Northwest Himalaya. *Tectonophysics*, *331*, 359–371.

Larson, K. M., Bürgmann, R., Bilham, R., & Freymuller, J. T. (1999). Kinematics of the India-Eurasia collision zone from GPS measurements. *Journal of Geophysical Research*, *104*, 1077–1093.

Lomax, A., Virieux, J., Volant, P., & Berge, C. (2000). Probabilistic earthquake location in 3D and layered models: Introduction of a Metropolis-Gibbs method and comparison with linear locations. In C. H. Thurber & N. Rabinowitz (Eds.), *Advances in Seismic Event Location* (Vol. 18, pp. 101–134). Netherlands: Kluwer Academic Publishers.

Malik, J. N., Sahoo, S., Satuluri, S., & Okumura, K. (2015). Active fault and paleoseismic studies in the Kangra Valley: Evidence of surface rupture of a great Himalayan 1905 Kangra earthquake (M_w 7.8), northwest Himalaya, India. *Bulletin of the Seismological Society of America*, *105*(5), 2325–2342.

McCaffrey, R., & Abers, J. (1988). *SYN3: A program for inversion of teleseismic body wave form on microcomputers* (Tech. Rep. AFGL-TR-0099 Air Force Geophysical Laboratory). Massachussets: Hanscomb Air Force Base.

McCaffrey, R., & Nabelek, F. (1987). Earthquakes, gravity and the origin of the Bali Basin: An example of a nascent continental fold-and-thrust belt. *Journal of Geophysical Research*, *92*, 441–460.

Mir, R. R., Parvez, I. A., Gaur, V. K., Ashish, R., & Romshoo, S. A. (2017). Chandra crustal structure beneath the Kashmir basin adjoining the Western Himalayan syntaxis. *Bulletin of the Seismological Society of America*, *107*(5), 2443–2458.

Mitra, S., Wanchoo, S., & Priestley, K. F. (2014). Source parameters of the 1 May 2013 M_b 5.7 Kishtwar earthquake: Implications for seismic hazards. *Bulletin of the Seismological Society of America*, *104*(2), 1013–1019.

Molnar, P. (1987). The distribution of intensity associated with the 1905 Kangra earthquake and bounds on the extent of the rupture zone. *Geological Society of India Version 1*, *29*(2), 221–229.

Nabelek, J. (1984). Determination of earthquake source parameters from inversion of body waves (Ph.D. thesis), Massachusetts Institute of Technology.

Paul, H., & Mitra, S. (2017). Three-dimensional crustal architecture beneath the Sikkim Himalaya and its relationship to active deformation. *Journal of Geophysical Research: Solid Earth*, *122*(10), 7860–7878.

Podvin, P., & Lecomte, I. (1991). Finite difference computation of traveltimes in very contrasted velocity models: A massively parallel approach and its associated tools. *Geophysical Journal International*, *105*, 271–284.

Rajendra Prasad, B., Klemperer, S. L., Vijay Rao, V., Tewari, H. C., & Khare, P. (2011). Crustal structure beneath the Sub-Himalayan fold-thrust belt, Kangra recess, northwest India, from seismic reflection profiling: Implications for late paleoproterozoic orogenesis and modern earthquake hazard. *Earth Planet Science Letters*, *308*, 218–228.

Rao, S. V. N., Rao, M. V., Ramasastri, K. S., & Singh, R. N. P. (1996). A study of sedimentation in Chenab Basin in Western Himalayas. *Hydrology Research*, *28*(3), 201–216.

Schiffman, C., Bali, B. S., & Bilham, R. (2011). *Seismic hazard implications of vanished Punjab mountain rammed 100 km beneath the south-east end of the Kashmir Valley*. San Francisco, Calif.: Abstract T54B-05 presented at 2011 Fall Meeting, AGU, 5-9 Dec.

Schiffman, C., Bali, B. S., Szeliga, W., & Bilham, R. (2013). Seismic slip deficit in the Kashmir Himalaya from GPS observations. *Geophysical Research Letters*, *40*, 5642–5645. https://doi.org/10.1002/2013GL057700

Searle, M., Waters, D., Rex, D., & Wilson, R. (1992). Pressure, temperature and time constraints on Himalayan metamorphism from eastern Kashmir and western Zanskar. *Journal of the Geological Society*, *149*(5), 753–773.

Sharma, S., Powali, D., Mitra, S., Wanchoo, S., Priestley, K., & Gaur, V. K (2018). *Lithospheric structure and earthquakes beneath Jammu and Kashmir Himalaya*. Vienna, Austria: Geophysical Research Abstracts, Vol. 20, EGU2018-11932, EGU General Assembly, 8-13 Apr.

Singh, K. (2010). Tectonic evolution of Kishtwar window with respect to the Main Central Thrust, northwest Himalaya. *India Journal of Asian Earth Sciences*, *39*, 125–135.

Sokos, E. N., & Zahradnik, J. (2008). ISOLA a Fortran code and a Matlab GUI to perform multiple-point source inversion of seismic data. *Computers & Geosciences*, *34*(8), 967–977.

Sokos, E. N., & Zahradnik, J. (2013). Evaluating centroid-moment-tensor uncertainty in the new version of ISOLA software. *Seismological Research Letters*, *84*, 656–665.

Stevens, V. L., & Avouac, J. P. (2015). Interseismic coupling on the main Himalayan thrust. *Geophysical Research Letters*, *42*, 5828–5837. https://doi.org/10.1002/2015GL064845

Szeliga, W., & Bilham, R. (2017). New constraints on the mechanism and rupture area for the 1905 M_w Kangra earthquake, northwest Himalaya. *Bulletin of the Seismological Society of America*, *107*(5), 2467–2479.

Szeliga, W., Hough, S., Martin, S., & Bilham, R. (2010). Intensity, magnitude, location, and attenuation in India for felt earthquakes since 1762. *Bulletin of the Seismological Society of America*, *100*(2), 570–584.

Tarantola, A., & Valette, B. (1982). Inverse problems = quest for information. *Journal of Geophysics*, *50*, 159–170.

Thakur, V. C. (1998). Structure of the Chamba nappe and position of the Main Central Thrust in Kashmir Himalaya. *Journal of Asian Earth Sciences*, *16*(2), 269–282.

Waldhauser, F., & Ellsworth, W. L. (2000). A double-difference earthquake location algorithm: Method and application to the Northern Hayward Fault, California. *Bulletin of the Seismological Society of America*, *90*(6), 1353–1368.

Wallace, K., Bilham, R., & Blume, F. (2005). Surface deformation in the region of the 1905 Kangra $M_w = 7.8$ earthquake in the period 1846–2001. *Geophysical Research Letters*, *32*, L15307.

Wang, K., & Bilek, S. (2011). Do subducting seamounts generate or stop large earthquakes? *Geology*, *39*(9), 819–822.

Wessel, P., & Smith, W. H. F. (1998). New, improved version of the generic mapping tools released. *Eos, Transactions of the American Geophysical Union*, *79*, 579.